Assessment of radionuclide transport uncertainty in the unsaturated zone of Yucca Mountain

Ming Ye [a,d], Feng Pan [a,d], Yu-Shu Wu [b,*], Bill X. Hu [c], Craig Shirley [a], Zhongbo Yu [d]

[a] *Division of Hydrologic Sciences, Desert Research Institute, Nevada System of Higher Education, Las Vegas, NV 89119, United States*
[b] *Earth Sciences Division, Lawrence Berkeley National Laboratory, Berkeley, CA 94720, United States*
[c] *Department of Geologic Sciences, Florida State University, Tallahassee, FL 32306, United States*
[d] *Department of Geosciences, University of Nevada, Las Vegas, NV 89119, United States*

Abstract

The present study assesses the uncertainty of flow and radionuclide transport in the unsaturated zone at Yucca Mountain using a Monte Carlo method. Matrix permeability, porosity, and sorption coefficient are considered random. Different from previous studies that assume distributions of the parameters, the distributions are determined in this study by applying comprehensive transformations and rigorous statistics to on-site measurements of the parameters. The distribution of permeability is further adjusted based on model calibration results. Correlation between matrix permeability and porosity is incorporated using the Latin Hypercube Sampling method. After conducting 200 Monte Carlo simulations of three-dimensional unsaturated flow and radionuclide transport for conservative and reactive tracers, the mean, variances, and 5th, 50th, and 95th percentiles for quantities of interest (e.g., matrix liquid saturation and water potential) are evaluated. The mean and 50th percentile are used as the mean predictions, and their associated predictive uncertainties are measured by the variances and the 5th and 95th percentiles (also known as uncertainty bounds). The mean predictions of matrix liquid saturation and water potential are in reasonable agreement with corresponding measurements. The uncertainty bounds include a large portion of the measurements, suggesting that the data variability can be partially explained by parameter uncertainty. The study illustrates propagation of predictive uncertainty of percolation flux, increasing downward from repository horizon to water table. Statistics from the breakthrough curves indicate that transport of the reactive tracer is delayed significantly by the sorption process, and prediction on the reactive tracer is of greater uncertainty than on the conservative tracer because randomness in the sorption coefficient increases the prediction uncertainty. Uncertainty in radionuclide transport is related to uncertainty in the percolation flux, suggesting that reducing the former entails reduction in the latter.
© 2006 Elsevier Ltd. All rights reserved.

Keywords: Monte Carlo simulation; Uncertainty analysis; Tracer and radionuclide transport; Parameter distribution function; Unsaturated zone; Yucca Mountain; Matrix permeability; Porosity; Sorption coefficient

1. Introduction

Yucca Mountain has been proposed by the US Department of Energy as the nation's long-term, permanent geologic repository for spent nuclear fuel or high-level radioactive waste. The potential repository would be located in Yucca Mountain's unsaturated zone (UZ),

which acts as a critical natural barrier delaying arrival of radionuclides to the water table. Since radionuclide transport in groundwater can pose serious threats to human health and the environment, it is indispensable to understand better flow and radionuclide transport in the UZ of Yucca Mountain. The UZ system consists of multiple hydrogeologic units whose hydraulic and geochemical properties exhibit both systematic and random spatial variation at multiple scales. Characterizing the heterogeneity and predicting radionuclide transport under such uncertain

---

* Corresponding author.
  E-mail address: YSWu@lbl.gov (Y.-S. Wu).

conditions is difficult, and this difficulty complicates decision making and risk analysis. Using stochastic methods, the present study assesses uncertainty in radionuclide transport caused by uncertainty in hydraulic and geochemical parameters used to model unsaturated flow and radionuclide transport in the Yucca Mountain UZ.

Since the 1980s, extensive field studies have been performed to collect various types of data for site characterization, and substantial numerical simulations have been conducted to understand flow and transport in the UZ. Recently, the hydrogeologic units of the UZ were characterized based on 4892 rock samples collected from the coring of 31 boreholes [7]. A database of hydraulic properties within the UZ zone was further developed based on 5320 core samples collected from 33 boreholes [8]. Hydraulic properties (e.g., permeability, porosity, and van Genuchten water retention parameters) of fracture and matrix in the UZ were compiled [17]. Sorption coefficients for a conservative tracer, technetium (^{99}Tc), and a reactive tracer, neptunium (^{237}Np) were measured for three types of rocks (devitrified, vitric, and zeolitc tuffs) in the UZ [27]. Since the 1990s, site-scale, three-dimensional (3-D) numerical models with high-spatial resolution have been developed to incorporate various physical processes [1,2,28,30–36]. Model calibrations have been conducted based on these site-scale models [1,3,25,28,30,31,45] and the importance of calibrating the site-scale, 3-D models to yield acceptable model predictions for the Yucca Mountain UZ has been shown [30,31,33–36].

The uncertainty of radionuclide transport caused by parameter randomness has been studied. Monte Carlo method was used by [22] to assess uncertainty in radionuclide travel time due to variations in recharge rate, matrix saturated hydraulic conductivity, porosity, and van Genuchten water retention parameters α and n. Since on-site parameter measurements of these variables at Yucca Mountain were limited before 1993, distributions of the parameters were simply assumed to be normal or lognormal. In addition, the Monte Carlo simulation in [22] was performed using a simple numerical model only for the Calico Hill nonwelded zeolitic layer of the UZ. A comprehensive uncertainty analysis is conducted in [45] by running Monte Carlo simulations using two-dimensional (2-D) random fields, generated from measured and calibrated matrix and fracture permeability and matrix van Genuchten α. 2-D Monte Carlo simulations were conducted in [12] by using random fields of heterogeneous fracture permeability and homogeneous matrix permeability. The random fields of fracture permeability were not generated based on site measurements at Yucca Mountain but on information obtained from the fractured tuff at the Apache Leap Research Site in central Arizona. As a summary, the previous uncertainty assessments were carried out only for part of the UZ using 2-D numerical models, whereas unsaturated flow and radionuclide transport actually occur in the heterogeneous 3-D UZ. In addition, previous studies simply assumed the distributions of model parameters and did not address the correlation between model parameters.

In the present study, we assess the uncertainty of unsaturated flow and radionuclide transport using a 3-D, site-scaled numerical model with random model parameters, based on site measurements and model calibration estimates. In addition, parameter correlation is also incorporated in the uncertainty assessment. The uncertainty analysis is conducted using a Monte Carlo method, which is conceptually straightforward and flexible to be applied to any known parameter distribution. Since this method is not limited to cases where parameter variance is small, it can be used as a reference to evaluate accuracy of various perturbation-based stochastic moment methods [6,9,42]. While the Monte Carlo method requires substantial computational resources, this limitation has become less critical over the last decade due to advances in computer hardware and software. Nevertheless, the Monte Carlo method still has several disadvantages. First, this method lacks theoretical convergence criteria for statistical moments higher than the mean. The common practice in resolving the convergence problem with Monte Carlo simulations is to examine stabilization of statistical moments at representative simulation locations and times. Second, the Monte Carlo method requires knowing the distributions of all random model parameters. In the present study, rigorous statistical methods are employed to identify model parameter distributions based on the results of site measurements and model calibrations instead of assuming the distributions, as in previous uncertainty analyses.

The uncertainty assessment is focused on predictive uncertainty in unsaturated flow and radionuclide transport caused by random matrix permeability, porosity, and sorption coefficient. Distributions of the three parameters are obtained based on site measurements of [7,17,27]. Uncertainty in the parameters, resulting from their spatial variability, can be quantified using measurements based on the ergodicity assumption. While the dual-continuum modeling approach used in the present study requires two sets of hydraulic properties for matrix and fracture media (see discussion in Section 2), matrix van Genuchten α and n are treated as deterministic variables, since their distributions cannot be rigorously identified for our 3-D uncertainty analysis based on limited site measurements. For example, only two or three measurement of the matrix van Genuchten α and n is available in each hydrogeologic unit. Other matrix parameters (e.g., residual saturation) are also handled deterministically in the present study, because they are less variable than the random matrix permeability, porosity, and sorption coefficient. Uncertainty of fracture properties is not assessed based on sensitivity analysis of [43], which shows that flow and transport simulations are not sensitive to fracture properties, because fracture flow dominates over the entire model domain. Another significant source of uncertainty in UZ modeling is the conceptualization of surface infiltration. Flow and transport processes under nine different infiltration

conditions were simulated [33,35,36]. The conceptual model uncertainty in surface infiltration is beyond the scope of the present study, although the uncertainty can be assessed by integrating the numerical simulation of [35,36] with the Maximum Likelihood Bayesian Model Averaging method recently developed [21,38].

Following a brief introduction in Section 2 of the computer model used for Monte Carlo simulations, we discuss methodologies and results of generating random fields of matrix permeability, porosity, and adsorption coefficient in Section 3. In Section 4, simulated flow variables (e.g., matrix liquid saturation and water potential) are compared with site measurements, and uncertainty in unsaturated flow and radionuclide transport is assessed. Conclusions are presented in Section 5.

2. Computer model

The computer model used in the present study is described briefly here, and more details can be found in [35]. The UZ of interest at Yucca Mountain is between 500 and 700 m thick and overlies a relatively flat water table. Yucca Mountain is a structurally complex geologic system of Tertiary volcanic rocks and heterogeneous environment of layered, anisotropic fractured tuff. Primarily based on the degree of formation welding, the geologic formations at Yucca Mountain have been organized into five major hydrogeologic units: Tiva Canyon welded (TCw) unit, Paintbrush nonwelded (PTn) unit, Topopah Spring welded (TSw) unit, Calico Hills nonwelded (CHn) unit, and Crater Flat undifferentiated (CFu) unit. The proposed repository would be located in the TSw unit. These five major units are divided further into about 30 subunits, which are associated with the computer layers in the numerical model. The 3-D model of the mountain-scale, unsaturated flow domain is discretized into a computational grid, which incorporates the layering heterogeneity at the site by representing each hydrogeologic subunit with several computational grid layers (at least one). The grid has an average of 45 vertical computational layers in the vertical direction and 980 columns (or gridblocks per layer) of both fracture and matrix continua, resulting in 86,400 gridblocks and 343,520 connections in a dual-permeability grid. It uses a refined mesh in the vicinity of the repository and includes every repository drift by taking account of orientations, lengths, elevations, and spacings of the drifts. Fig. 1 is the plan view of the grid and shows the plotted model domain, faults, proposed repository layout, and locations of several boreholes.

The dual-continuum approach is used in the modeling. Two sets of properties (i.e., relative permeability and capillary pressure curves), along with other intrinsic properties (e.g., permeability, porosity, density, fracture geometric parameters, and transport properties) are needed for the two media of fractured and matrix systems. Because the van Genuchten model of relative permeability and capillary pressure functions is used to describe variably saturated
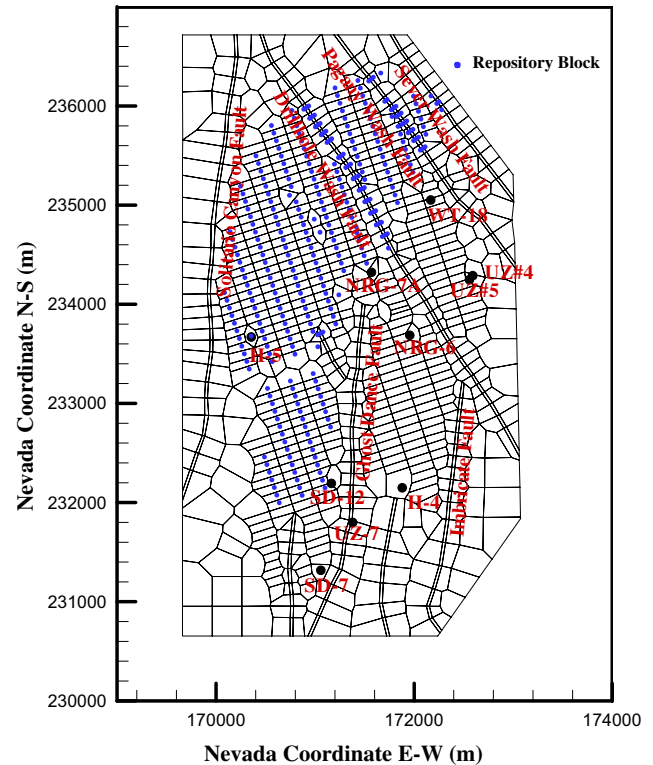

Fig. 1. Plan view of the 3-D UZ model grid shows the model domain, faults, proposed repository layout, and locations of several boreholes.

flow in both fracture and matrix continua, the basic rock and flow parameters used for each model layer include (a) fracture properties (frequency, spacing, porosity, permeability, van Genuchten α and n parameters, residual saturation, and fracture–matrix interface area); (b) matrix properties (porosity, permeability, van Genuchten α and n parameters, and residual saturation); (c) transport properties (grain density, diffusion, adsorption, and tortuosity coefficients); and (d) fault properties (porosity, matrix and fracture permeability, and active fracture–matrix interface area). As discussed in Section 1, only matrix permeability, porosity, and adsorption coefficient are treated as random variables in the present study. For each of the computational layers, equally likely random parameter samples drawn from parameter distributions identified in Section 3 are assigned to all gridblocks within the layer.

The unsaturated flow module, EOS9 (solving Richards' equation), of TOUGH2 [24] is used to simulate moisture movement in the UZ, which is approximated at a quasi-steady-state or steady-state condition. Another TOUGH2-family code, T2R3D [32], is used for modeling radionuclide transport through fractured tuffs. For the flow model, the ground surface and water table are taken as top and bottom boundaries, which are treated as Dirichlet-type conditions with specified pressure or saturation values. All lateral boundaries are treated as no-flow (closed) boundaries. A present-day, net infiltration estimate used in [35] (Fig. 2) is applied as a source term in the fracture gridblocks within the second grid layer from the top, since
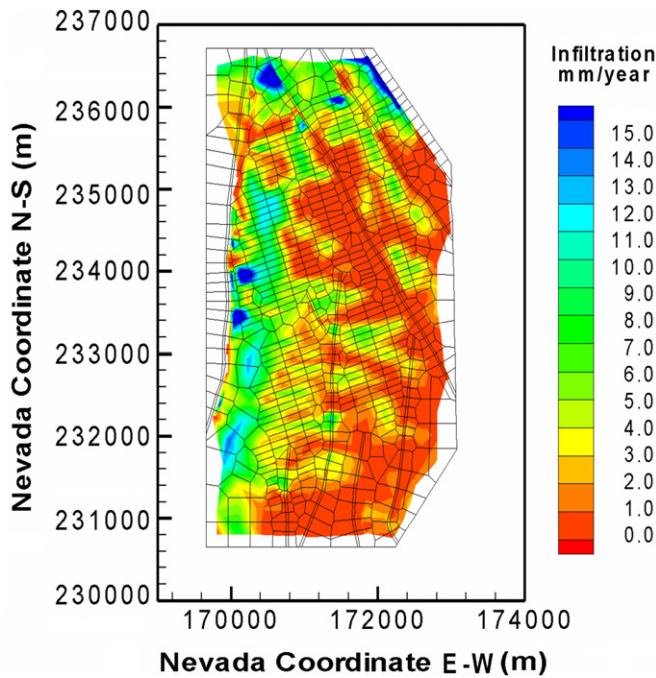
Fig. 2. Plan view of present-day net infiltration distributed over the 3-D unsaturated zone flow model grid.

the first layer is treated as a Dirichlet boundary to represent average atmospheric conditions on the land surface. Net infiltration from precipitation is the major control on overall hydrologic and thermal-hydrologic conditions within the UZ.

3. Generation of correlated random fields

After introducing methodologies for identifying parameter distributions and generating correlated random fields based on parameter site measurements, the identified parameter distributions and generated parameter fields are discussed in this section. Measurements of matrix permeability (transferred from the saturated hydraulic conductivity measured from core samples) and porosity compiled by [17] are used in the present study. Distribution identification and random generation are first applied to the measured hydraulic conductivity, and then the generated conductivity is transferred to permeability for TOUGH2 numerical simulations. Measurements of sorption coefficients for the reactive tracer, neptunium (^{237}Np), in three types of representative rocks, (devitrified, vitric, and zeolitc tuffs) are compiled from [27]. Descriptive statistics of these measurements are referred to [17,23].

3.1. Identification of parameter distributions

Since parameter measurements are seldom adequate to describe the corresponding parameter distribution without appropriate transforms [5], three distribution types of transformations (lognormal, log ratio, and hyperbolic arc-

sine) from the Johnson system [5,15] and four classical re-expressions ($1/X$, $X^{1/2}$, $X^{1/3}$, X^2) [18] are selected to transform the parameter measurements. The seven transformations include all transformations reported in literature dealing with distributions of hydraulic parameters of unsaturated media. The lognormal (LN), log ratio (SB), and hyperbolic arcsine (SU) transforms are given as follows [5]:

$$LN : \ Y = \ln(X) \tag{1}$$

$$SB : \ Y = \ln\left(\frac{X - A}{B - X}\right) \tag{2}$$

$$SU : \ Y = \sinh^{-1}(U) = \ln(U + \sqrt{1 + U^2}) \tag{3}$$

where X is the untransformed variable value with limits of variation from A to B ($A < X < B$) and $U = (X - A)/(B - A)$. Another distribution is the Gaussian distribution denoted by NO, meaning no transform. The best one among the eight distributions (NO, LN, SB, SU, $1/X$, $X^{1/2}$, $X^{1/3}$, and X^2) is selected using the Lilliefors goodness-of-fit test for normality, a variant of the Kolmogorov–Smirnov (K–S) test. Different from the K–S test, the Lilliefors test does not require a hypothesized distribution with mean and variance (or more rigorously, cumulative distribution function) specified a priori. Instead, mean and variance in the Lilliefors test are estimated from measurements [4]. The Lilliefors test is implemented in the following three steps:

(1) Standardize transformed measurements y_i with their sample mean, $\overline{Y}$, and standard deviation, s; i.e., $z_i = (y_i - \overline{Y})/s$ ($i = 1, 2, \ldots, N$), where N is the sample size (at least 4 for the Lilliefors test [4]).
(2) Calculate the empirical cumulative distribution function (CDF), $G(Z)$, of the standardized variable Z and standard normal CDF, $F^*(Z)$; estimate the maximum absolute difference, $T = \max|F^*(z_i) - G(z_i)|$ ($i = 1, 2, \ldots, N$), between $G(Z)$ and $F^*(Z)$.
(3) Select the Lilliefors test statistic T^* corresponding to a level of significance α from the Lilliefors Test Statistical Table [4]. If T exceeds T^*, reject the hypothesis of normality at the significance level of α.

While application of the Lilliefors test for normal, lognormal, and beta distributions was proposed also by [20], the Lilliefors test for normality appears sufficient in this study.

3.2. Latin Hypercube Sampling and rank correlation

The Latin Hypercube Sampling (LHS) method [10,19] is used to generate correlated random fields of permeability and porosity in the present study. The correlation between permeability and sorption coefficient cannot be estimated, since they were measured by different researchers at separate locations, and the data pairs of the two parameters

are not available. Permeability and porosity were measured by [7] together, and data pairs of the two parameters exist. LHS is selected for random field generation since it ensures that generated random samples span the full coverage of a random variable obtained from parameter measurements, even when the sample size is relatively small. This property of LHS reduces the computational cost of Monte Carlo simulations, since in comparison with the random sampling method, LHS requires a smaller number of parameter realizations to yield representative parameter distribution functions [10,44]. Another advantage of LHS is that it can easily incorporate parameter correlations into the generated random fields. The Spearman rank correlation coefficient, RCC_{XY}, proposed by [13] is used in the present study to measure the correlation between two random variables X and Y. The Spearman rank correlation coefficient is defined as follows [10]:

$$RCC_{XY} = \frac{\sum_{i=1}^{N} \left[R(x_i) - \overline{R}(X)\right]\left[R(y_i) - \overline{R}(Y)\right]}{\left\{\sum_{i=1}^{N}\left[R(x_i) - \overline{R}(X)\right]^2\right\}^{1/2}\left\{\sum_{i=1}^{N}\left[R(y_i) - \overline{R}(Y)\right]^2\right\}^{1/2}}$$
$$= 1 - 6\sum_{i=1}^{N}\frac{\left[R(x_i) - R(y_i)\right]^2}{N(N^2 - 1)} \quad (4)$$

where $R(x_i)$ and $R(y_i)$ are the ranking indexes of x_i and y_i in ascending order, respectively; N is the sample size; and the mean rank is $\overline{R}(X) = \overline{R}(Y) = (N + 1)/2$. The technique of rank correlation is distribution-free and can incorporate the correlation information better than the commonly used Pearson correlation coefficient [10]. In the present study, the correlation between the selected best distributions of permeability and porosity (not the original ones) are estimated. The LHS code of [14] is used to generate random fields; this code requires the first and 99th percentiles of a normal distribution as inputs, which are estimated as follows [26]:

$$V_{0.01} = \mu - 2.326\sigma \quad \text{and} \quad V_{0.99} = \mu + 2.326\sigma \quad (5)$$

where μ and σ are the mean and standard deviations of a normal distribution. After the random fields corresponding to the selected best transforms are generated, the generated random fields need to be transformed back to their original scale, using one of the following equations:

$$LN: \ X = \exp(Y) \quad (6)$$
$$SB: \ X = [B\exp(Y) + A]/[1 + \exp(Y)] \quad (7)$$
$$SU: \ X = A + (B - A)[\exp(Y) - \exp(-Y)]/2 \quad (8)$$
$$X = 1/Y; \quad X = Y^2; \quad X = Y^3; \quad X = Y^{1/2} \quad (9)$$

where Y is the transformed value generated by LHS, and X is the parameter value in its original scale.

3.3. Results of distribution identification

For the saturated hydraulic conductivity, Table 1 lists the values of A and B needed for the SB and SU trans-

forms; selected best distributions based on the Lilliefors test; mean and variance of the transformed data; maximum absolute distribution difference, T; and Lilliefors criteria, T^*, for significance levels of 0.01, 0.05, and 0.1. The first column in Table 1 lists the names of hydrogeologic units used in the numerical modeling. The Lilliefors test is not applied to select the best distribution for the six units of CCR&CUC, TPY, PV2a, BTv and BF2, since there are fewer than four measurements in each of the units (matrix permeability in the six units is thus fixed consequently in Monte Carlo simulations). For the units of PV2v, CHV, and CHZ, as suggested by [5], a few outliers are excluded from the estimations of mean and variance to yield a better distribution fit, whereas the outliers are still included in the calculation of the maximum absolute distribution difference (T). For the units of CNW, BT4, BT3, BT2, and BF3, the best distribution yields a negative 1st percentile, $V_{0.01}$, calculated by Eq. (4) and thus is not selected. Instead, the second best fit is selected. Eighty percent of the selected best distributions are determined at the significance level of 0.05 in the Lilliefors normality test. Whereas the normality assumption is rejected in the two units of TMN and CHZ at all significance levels, the distribution with the smallest value of T is selected, which appears acceptable because of the small difference between the empirical and theoretical CDFs, $G(Z)$ and $F^*(Z)$, shown in Fig. 3. The logarithm transform (LN) is the best distribution for the saturated hydraulic conductivity for 14 of the total 25 tested hydrogeologic units.

Table 2 lists the statistical parameters of distribution approximation for matrix porosity in the same manner as Table 1, and no dominating transformation is found. More measurements of porosity are available than those of saturated hydraulic conductivity in each hydrogeologic unit, and the procedure of distribution identification cannot be applied only for the unit of BTv, owning to the lack of measurements in BTv. The footnote below the table gives the details for the distribution selection. While 28 distributions are accepted at various significance levels, no best distribution can be accepted for the four units of CUL&CW, TMN, TM2&TM1, and CHZ. This may be attributed to the large sample sizes (ranging from 277 to 694) in these units, since the Lilliefors criteria, T^*, are inversely proportional to the square root of the sample size. The transform with the smallest T, however, is accepted in the study, because of the small difference between the empirical and theoretical CDFs, $G(Z)$ and $F^*(Z)$, shown in Fig. 3.

Table 3 displays the Spearman rank correlations between the transformed matrix porosity and saturated hydraulic conductivity. Note that the data pairs between the two parameters are significantly less than the measurements of individual parameters. In addition, the Spearman rank correlation cannot be estimated for hydrogeologic units of CCR&CUC, TPY, PV2a, BTv, and BF2 because of the small number of data pairs. The rank correlations are used by the LHS code to generated correlated random

Table 1
Statistical parameters of matrix saturated hydraulic conductivity for distribution approximation

Hydrogeologic units	Limits of variation		Transform	Estimated distribution			Critical value (T^*)		
	A	B		Mean	Variance	T	$\alpha = 0.10$	$\alpha = 0.05$	$\alpha = 0.01$
CCR&CUC[a]									
CUL&CW	2.48E−13	1.25E−08	LN	−25.40	8.37	0.140	0.189	0.206	0.245
CMW	3.33E−12	9.42E−08	SB	−6.06	67.5	0.323	0.315	0.337	0.405
CNW[c]	5.11E−12	8.80E−07	LN	−18.2	22.2	0.235	0.239	0.258	0.294
BT4[c]	1.79E−10	2.55E−05	LN	−14.2	10.6	0.207	0.230	0.249	0.284
TPY[a]									
BT3[c]	1.89E−09	7.31E−06	$X^{1/3}$	1.04E−02	2.40E−06	0.236	0.230	0.249	0.284
TPP	8.99E−08	1.75E−06	SB	0.754	16.9	0.209	0.230	0.249	0.284
BT2[c]	1.23E−09	2.07E−05	LN	−13	6.61	0.192	0.171	0.187	0.225
TC	1.69E−11	1.69E−07	SB	−5.23	42.8	0.172	0.294	0.319	0.364
TR	1.69E−11	9.38E−06	LN	−20.3	4.47	0.133	0.117	0.129	0.150
TUL	4.19E−13	1.43E−06	LN	−22.8	7.29	0.163	0.132	0.146	0.169
TMN	4.75E−13	1.24E−09	LN	−25.8	2.32	0.134	0.094	0.103	0.120
TLL	1.38E−12	7.66E−08	LN	−22.3	6.42	0.096	0.112	0.123	0.143
TM2&TM1	5.32E−13	9.40E−06	SB	−12.4	33.4	0.140	0.168	0.183	0.219
PV3	8.62E−14	2.26E−09	LN	−25.8	7.25	0.154	0.189	0.206	0.245
PV2a[a]									
PV2v[b]	5.02E−11	1.21E−05	$X^{1/3}$	1.26E−02	1.26E−05	0.211	0.195	0.213	0.250
BT1a	1.82E−13	8.71E−08	SB	−7.16	59.2	0.189	0.239	0.258	0.294
BT1v	1.03E−10	2.21E−05	LN	−14.1	6.48	0.131	0.136	0.150	0.174
CHV[b]	1.67E−12	7.21E−05	$X^{1/3}$	0.0168	1.34E−04	0.144	0.117	0.129	0.150
CHZ[b]	3.87E−13	9.55E−08	LN	−24.1	1.83	0.118	0.081	0.089	0.104
BTa	2.07E−13	2.11E−10	SB	−3.80	26.3	0.182	0.249	0.271	0.311
BTv[a]									
PP4	8.43E−13	3.09E−07	SB	−7.11	52.3	0.239	0.261	0.285	0.331
PP3	4.19E−12	3.66E−07	$X^{1/3}$	3.72E−03	1.62E−06	0.114	0.113	0.124	0.144
PP2	3.74E−12	1.16E−08	LN	−22.2	5.05	0.101	0.136	0.150	0.174
PP1	1.69E−12	1.95E−06	LN	−22.6	10.4	0.149	0.152	0.167	0.195
BF3[c]	6.89E−11	5.59E−08	LN	−20.0	7.32	0.191	0.276	0.300	0.348
BF2[a]									

[a] The sample size is less than 4 and cannot fit the distribution using Lilliefors Test in the layers.
[b] The outlying values were discarded, but were included for goodness of fit calculation in the layer.
[c] The distribution is not the best fit in order to guarantee the reasonable ranges of random fields.

fields of matrix porosity and saturated hydraulic conductivity, which subsequently transferred to permeability.

Table 4 presents the statistical parameters of distribution approximation for the sorption coefficient of the reactive tracer neptunium (^{237}Np) in the same manner as Tables 1 and 2. The best distributions of the sorption coefficients for the three rock types of devitrified, vitric, and zeolitic tuff are selected based on the Lilliefors test at a significance level of 0.05. For two of the three rock types, the logarithm transform is found to be the best distribution for the sorption coefficient.

Fig. 3 plots the empirical CDF, $G(Z)$, of the selected best distribution and the theoretical CDF, $F^*(Z)$, of (a–b) matrix hydraulic conductivity, (c–f) matrix porosity, and (g–i) sorption coefficient of neptunium (^{237}Np). Such plots for saturated hydraulic conductivity and porosity in all hydrogeologic units are referred to [23]. Fig. 3 shows that $G(Z)$ agrees well with $F^*(Z)$, indicating the selected distributions are appropriate. In particular, Fig. 3a and b plot the CDFs of the saturated hydraulic conductivity for the two hydrogeologic units of TMN and CHZ, where the nor-

mality assumption is rejected for all eight distributions at all three significance levels. Fig. 3c–f do the same for the matrix porosity in the four composite units of CUL&CW, TMN, TM2&TM1, and CHZ. Fig. 3a–f show that $G(Z)$ slightly deviates from $F^*(Z)$, especially for matrix porosity (Fig. 3c–f), suggesting that the selected best distribution is acceptable.

3.4. Results of random field generation

Two hundred realizations of saturated hydraulic conductivity, porosity, and sorption coefficients of neptunium (^{237}Np) are generated using the Latin Hypercube Sampling method for all hydrogeologic units, except for the units with less than four measurements. Fig. 4 plots relative frequencies of measured and generated (a–b) log matrix saturated hydraulic conductivity, (c–d) matrix porosity for the two units of TMN and CHZ, and (e–f) sorption coefficient of neptunium (^{237}Np) for two rock types of devitrified and vitric tuff. Such plots for saturated hydraulic conductivity and porosity in all the hydrogeologic units and rock types
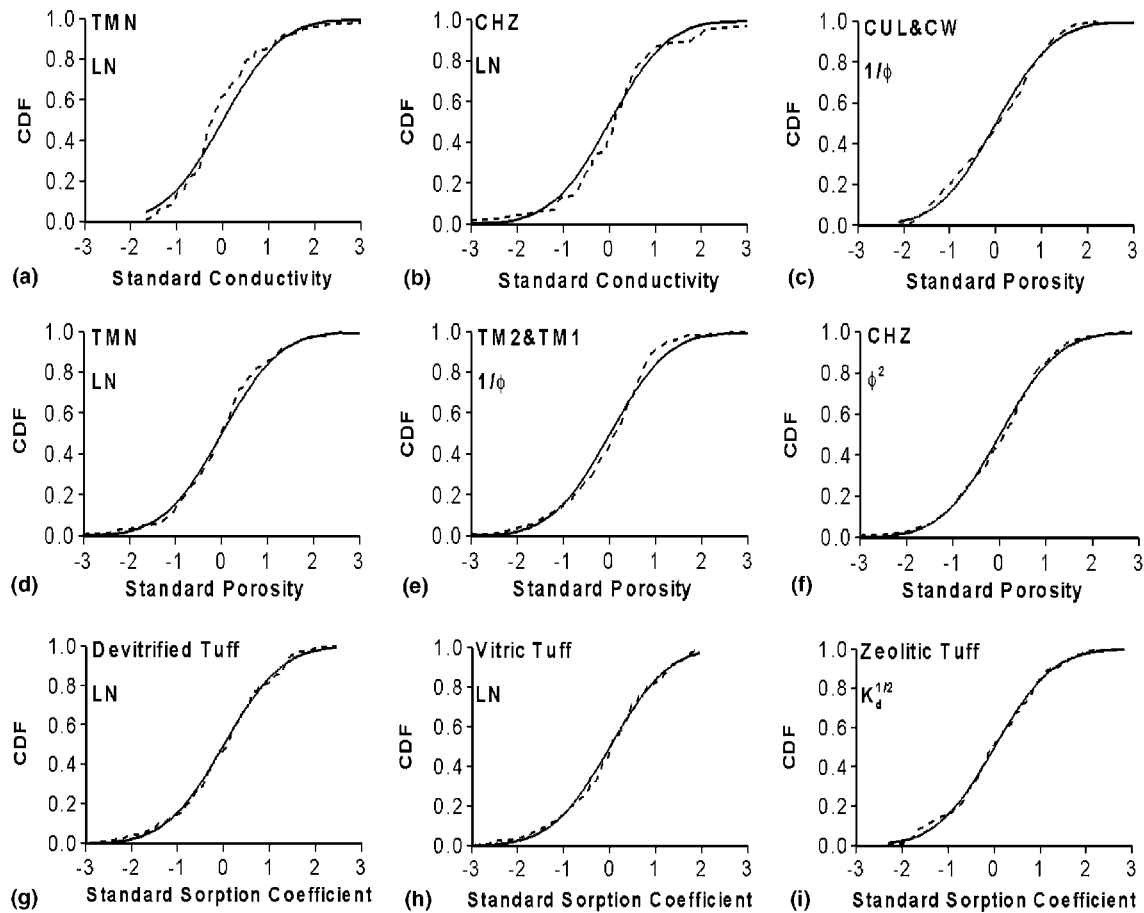
Fig. 3. Empirical (dashed) and theoretical (solid) cumulative distribution functions (CDF) for transformed (a,b) matrix saturated hydraulic conductivity, (c–f) matrix porosity, and (g–i) sorption coefficient of neptunium (^{237}Np) in three selected hydrogeologic units. The selected best distributions are listed in the figures.

are referred to [23]. Fig. 4 shows that the distributions of generated parameters agree well with the corresponding measurements, even in the units of TMN and CHZ, where the normality assumption is rejected for all distributions.

Previous modeling [30,31,35,36] has shown that parameters measured in the field and laboratory, and/or parameters estimated by one-dimensional models, cannot be used directly by 3-D models to produce acceptable simulation results. This is due to model uncertainty and the different spatial–temporal scales between model input parameters and their measured and estimated values. Instead, the parameter set of permeability obtained from both parameter measurements and 3-D model calibrations [3,16] were employed for the numerical simulations [35,36]. Their simulations appear reasonable in comparison with field measurements of water saturation and potential.

In the present study, the model inputs of permeability used by [35,36] are included in the range (between the minimum and maximum) of measured permeability in almost all hydrogeologic units. Nevertheless, in the units of BT3, TPP, CHV, PP3, and BF2, the model inputs are larger than the maximum measurements. To yield better simulations,

the model inputs of [35,36] in these units are assumed to be the means of saturated hydraulic conductivity. The associated variances are adopted from those determined by the Lilliefors test after appropriate transforms, given in Table 1. Since the distributions of matrix saturated hydraulic conductivity cannot be identified in the hydrogeologic units of CCR&CUC, TPY, PV2a, BTv, and BF2 because of their small sample size (fewer than four), matrix hydraulic conductivity in these units is treated as a deterministic variable having the values of model inputs given in [35]. Fig. 5a and b plots the mean, maximum, and minimum logarithm of measured and generated permeability, respectively, for all hydrogeologic units. Fig. 5b shows that the model inputs from [35,36] are within the ranges of generated permeability but are not identical with their means. Mean permeability in Fig. 5a differs from that in Fig. 5b for certain units due to the use of calibrated permeability as the mean, as discussed previously. In Fig. 5a and b, the differences in range of permeability for certain hydrogeologic units is caused by the exclusion of measurement outliers from estimates of mean and variance, as discussed in Section 3.3. For example, in the hydrogeologic units of CHV and

Table 2
Statistical parameters of matrix porosity for distribution approximation

Hydrogeologic units	Limits of variation		Transform	Estimated distribution			Critical values (T^*)		
	A	B		Mean	Variance	T	$\alpha = 0.10$	$\alpha = 0.05$	$\alpha = 0.01$
CCR&CUC[a]	0.037	0.432	X^2	0.063	6.58E−04	0.078	0.072	0.080	0.093
CUL&CW	0.031	0.214	$1/X$	12.63	14.20	0.072	0.031	0.034	0.039
CMW	0.099	0.453	$1/X$	5.300	1.49	0.085	0.087	0.090	0.105
CNW	0.227	0.634	NO	0.387	4.74E−03	0.057	0.079	0.087	0.101
BT4	0.133	0.670	SU	0.520	2.63E−02	0.117	0.106	0.116	0.135
TPY	0.072	0.310	X^2	0.058	5.84E−04	0.106	0.129	0.142	0.165
BT3	0.136	0.579	SU	0.585	2.50E−02	0.084	0.094	0.104	0.121
TPP	0.387	0.624	$1/X$	2.021	2.56E−02	0.060	0.064	0.070	0.082
BT2[a]	0.103	0.615	SB	1.385	0.79	0.073	0.061	0.067	0.078
TC	0.011	0.274	$X^{1/3}$	0.365	4.66E−03	0.059	0.093	0.102	0.119
TR	0.061	0.268	NO	0.157	8.75E−04	0.048	0.038	0.042	0.049
TUL	0.075	0.251	NO	0.155	9.28E−04	0.044	0.038	0.042	0.049
TMN	0.054	0.193	LN	−2.218	3.29E−02	0.070	0.048	0.053	0.062
TLL	0.087	0.264	$1/X$	8.012	2.55	0.044	0.036	0.040	0.046
TM2&TM1	0.052	0.342	$1/X$	10.11	3.23	0.082	0.046	0.051	0.060
PV3	0.010	0.341	SB	−2.728	2.04	0.060	0.072	0.079	0.092
PV2a[b]	0.109	0.416	SB	0.181	6.77	0.191	0.214	0.234	0.268
PV2v	0.047	0.471	SB	−0.311	3.79	0.123	0.115	0.127	0.147
BT1a	0.157	0.401	$X^{1/3}$	0.656	1.58E−03	0.061	0.119	0.131	0.152
BT1v[b]	0.030	0.501	NO	0.324	7.20E−03	0.088	0.090	0.099	0.115
CHV[a]	0.037	0.491	$1/X$	2.944	0.079	0.061	0.071	0.078	0.090
CHZ	0.098	0.434	X^2	0.106	8.30E−04	0.068	0.035	0.039	0.045
BTa	0.180	0.419	$1/X$	3.791	0.40	0.064	0.094	0.104	0.121
BTv[c]									
PP4	0.215	0.441	NO	0.327	2.49E−03	0.049	0.108	0.118	0.138
PP3	0.245	0.396	NO	0.318	9.94E−04	0.054	0.062	0.068	0.080
PP2	0.098	0.334	NO	0.221	3.37E−03	0.066	0.071	0.079	0.091
PP1	0.163	0.427	X^2	0.090	6.21E−04	0.050	0.049	0.053	0.062
BF3[a]	0.058	0.370	$1/X$	8.573	9.40	0.078	0.079	0.086	0.101
BF2	0.159	0.330	$1/X$	4.451	0.81	0.095	0.127	0.140	0.163

[a] The outlying values were discarded but were included for goodness of fit calculation in the layer.
[b] The distribution is not best fit in order to guarantee the reasonable ranges of random fields.
[c] The sample size is less than 4 and cannot fit the distribution using Lilliefors Test in the layers.

Table 3
Spearman rank correlation between the transformed matrix saturated conductivity and matrix porosity

Hydrogeologic units	Spearman rank correlation	Sample size	Hydrogeologic units	Spearman rank correlation	Sample size
CCR&CUC[a]		3	PV3	−0.20	17
CUL&CW	−0.50	17	PV2a[a]		1
CMW	0.60	5	PV2v	0.06	16
CNW	0.61	10	BT1a	0.12	10
BT4	0.26	11	BT1v	0.37	35
TPY[a]		2	CHV	−0.19	47
BT3	0.03	11	CHZ	0.47	99
TPP	−0.47	11	BTa	0.22	9
BT2	0.42	21	BTv[a]		1
TC	−0.49	6	PP4	0.52	8
TR	0.39	47	PP3	0.45	51
TUL	0.40	37	PP2	0.68	35
TMN	0.48	9	PP1	0.24	28
TLL	−0.46	52	BF3	−0.71	7
TM2&TM1	−0.39	22	BF2[a]		1

[a] Spearman rank correlation coefficient cannot be estimated due to the lack of data pairs between the two parameters.

CHZ, deleting the outliers results in a smaller variance in permeability, which causes the smaller ranges of the generated data than the measurements. While the mean sorption coefficients of neptunium (^{237}Np) are smaller than those used by [35], they are not adjusted because no calibrated sorption coefficients are available.

Table 4
Statistical parameters of sorption coefficient of neptunium for distribution approximation

Materials	Limits of variation		Transform	Estimated distribution			Critical values (T^*)		
	A	B		Mean	Variance	T	$\alpha = 0.10$	$\alpha = 0.05$	$\alpha = 0.01$
Devitrified tuff	0.007	8.236	LN	−1.06	1.67	0.0396	0.0527	0.0580	0.0675
Vitric tuff	0.018	4.072	LN	−0.73	1.18	0.0588	0.0548	0.0603	0.0702
Zeolitic tuff	0.031	8.743	$X^{1/2}$	1.43	0.293	0.0382	0.0495	0.0545	0.0635
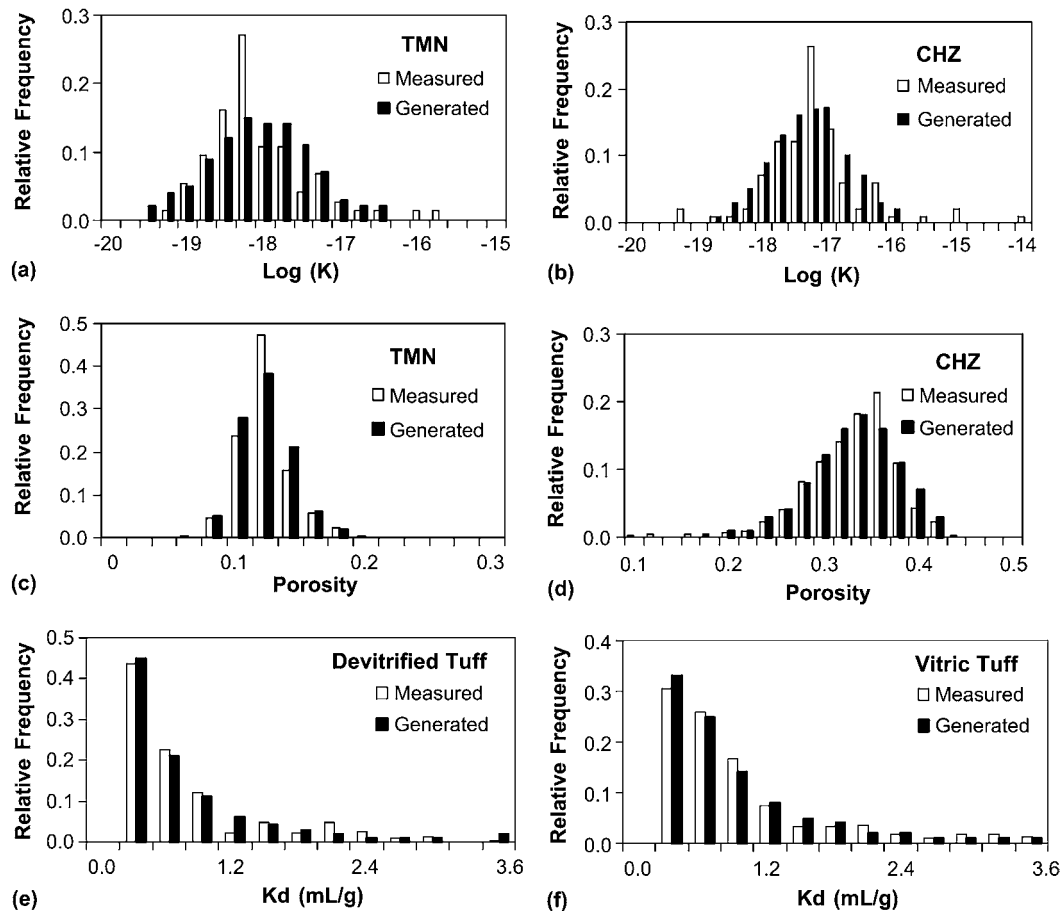
Fig. 4. Histograms of measured and generated (a,b) log saturated matrix hydraulic conductivity, (c,d) matrix porosity in two hydrogeologic units, and (e,f) sorption coefficient of neptunium (^{237}Np).

4. Simulation results and discussions

After conducting 200 Monte Carlo simulations using the TOUGH2 modules of EOS9 and T2R3D, similar to [39], convergence of the 200 simulations is investigated empirically by examining stabilization of the mean and variance in the simulated variables (i.e., saturation, capillary pressure, percolation flux, and concentration) at representative locations and times. The examination shows that the 200 simulations are sufficient to yield meaningful sample statistics for assessing prediction and uncertainty. Mean, variance, and 5th, 50th, and 95th percentiles in quantities of interest (e.g., saturation, water flux, and concentration)

are estimated from Monte Carlo results. Since the predicted quantities may not follow normal distributions, the 5th and 95th percentiles (also known as uncertainty bounds) are superior to 95% of confidence intervals calculated based on mean and variance to quantify uncertainty of radionuclide transport in unsaturated flow. Therefore, for all figures below, in addition to mean and variance used to present the average estimates and associated predictive uncertainty, 5th and 95th percentiles also are plotted to assess uncertainty. The deterministic simulation results of [35] are treated in this the present analysis as a baseline case to compare stochastic simulations. Note, as shown in Fig. 5b, that the means of the random parameters used
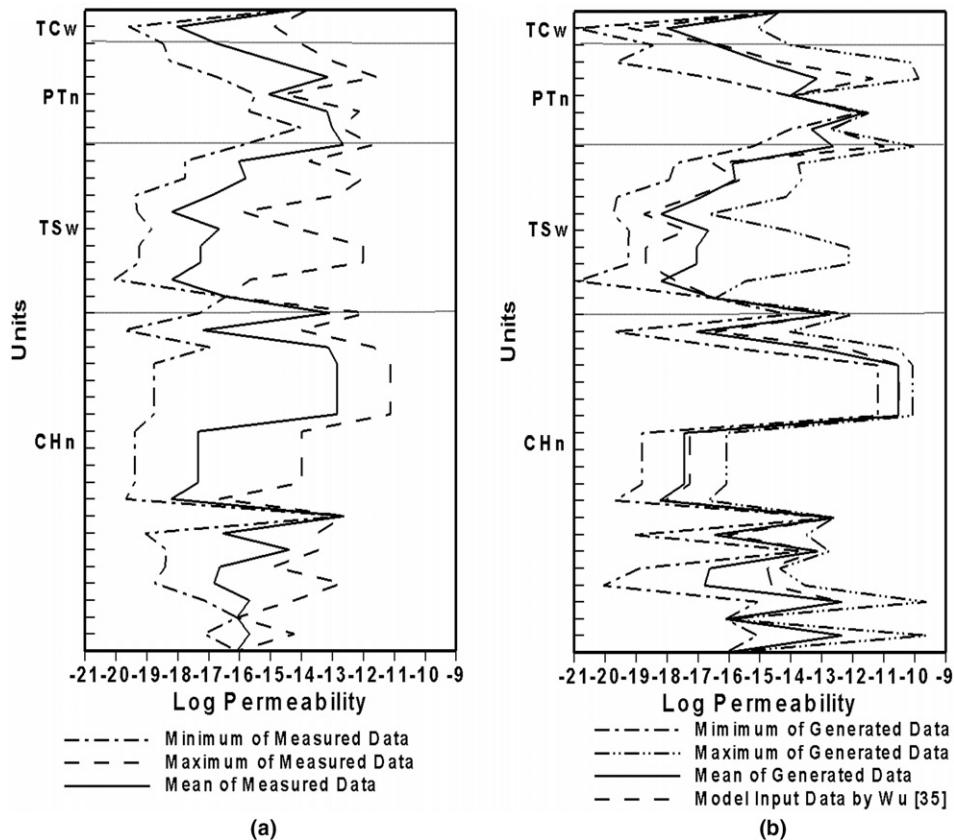
Fig. 5. Comparison of (a) measured and (b) simulated log matrix permeability. The model inputs of Wu et al. [35] are plotted in (b).

for the stochastic simulations differ from the model inputs of [35].

4.1. Uncertainty assessment of unsaturated flow

Statistics of matrix liquid saturation, water potential, and percolation flux are estimated based on the 200 Monte Carlo simulations. After comparing statistics of the former two variables with corresponding site measurements, the spatial flow pattern of percolation flux and associated predictive uncertainty is assessed.

4.1.1. Comparisons with saturation and water potential measurements

Fig. 6 compares the observed and 3-D simulated matrix liquid saturation along borehole SD-12. Fig. 7 does the same for water potential. In each figure, the mean and 50th-percentile predictions are close but not identical, suggesting that simulated variables may not follow normal distributions. Nonstationary behavior of matrix liquid saturation and water potential are observed in Figs. 6 and 7, which can be simulated with nonstationary stochastic moment equations approaches of [11,29,37,40,41]. The mean and 50th-percentile predictions deviate from the corresponding results of the deterministic case. This is not surprising because, as discussed in Section 3.4, the mean model parameters used for the stochastic analyses are dif-
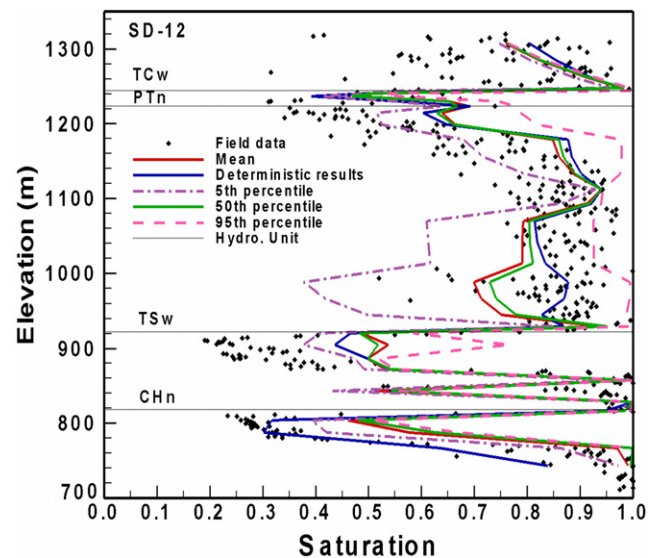

Fig. 6. Comparison of observed and 3-D model simulated matrix liquid saturation for borehole SD-12.

ferent from the model inputs for the deterministic case. The 5th and 95th percentiles (also known as uncertainty bounds) of simulated matrix liquid saturation and water potential bracket a significant number of measurements, indicting the data variability can be partially explained by parametric uncertainty in the matrix permeability and
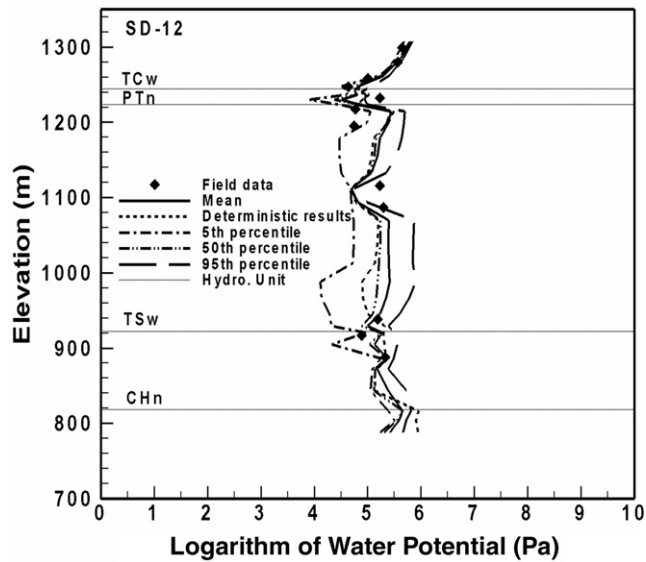
Fig. 7. Comparison to observed and 3-D model simulated water potentials for borehole SD-12.

porosity. In particular, certain measurements that cannot be caught by deterministic simulation (e.g., matrix liquid saturation at the bottom of TSw) are included in the uncertainty bounds. This is particularly true for the comparison of water potential shown in Fig. 7. Nevertheless, the results of the deterministic case match the trend for measurements to be better at the bottom of hydrogeologic units TSw and CHn than at the mean and 50th percentile in the stochastic predictions, suggesting that more calibration information should be included in stochastic simulations. Unbracketed measurements can be attributed to measurement error, conceptual model incompleteness, and different scales between model inputs and field and laboratory parameter measurements. Simulated and measured matrix liquid saturations also are compared along boreholes UZ-14 and SD-7 (not shown here), where more measurements are bracketed by the 5th and 95th percentiles [23].

4.1.2. Flow pattern and uncertainty assessment

Percolation flux through the UZ is considered one of the most critical factors affecting performance in the proposed repository drifts. The percolation flux, defined in the present study as the total vertical liquid mass flux through both fracture and matrix, is converted to millimeters per year using a constant water density. Since the lateral boundaries of the model domain are impermeable, the percolation flux is driven by the surface infiltration (Fig. 2). Fig. 8 plots (a) mean, (b) variance, (c) 5th percentile, and (d) 95th percen-
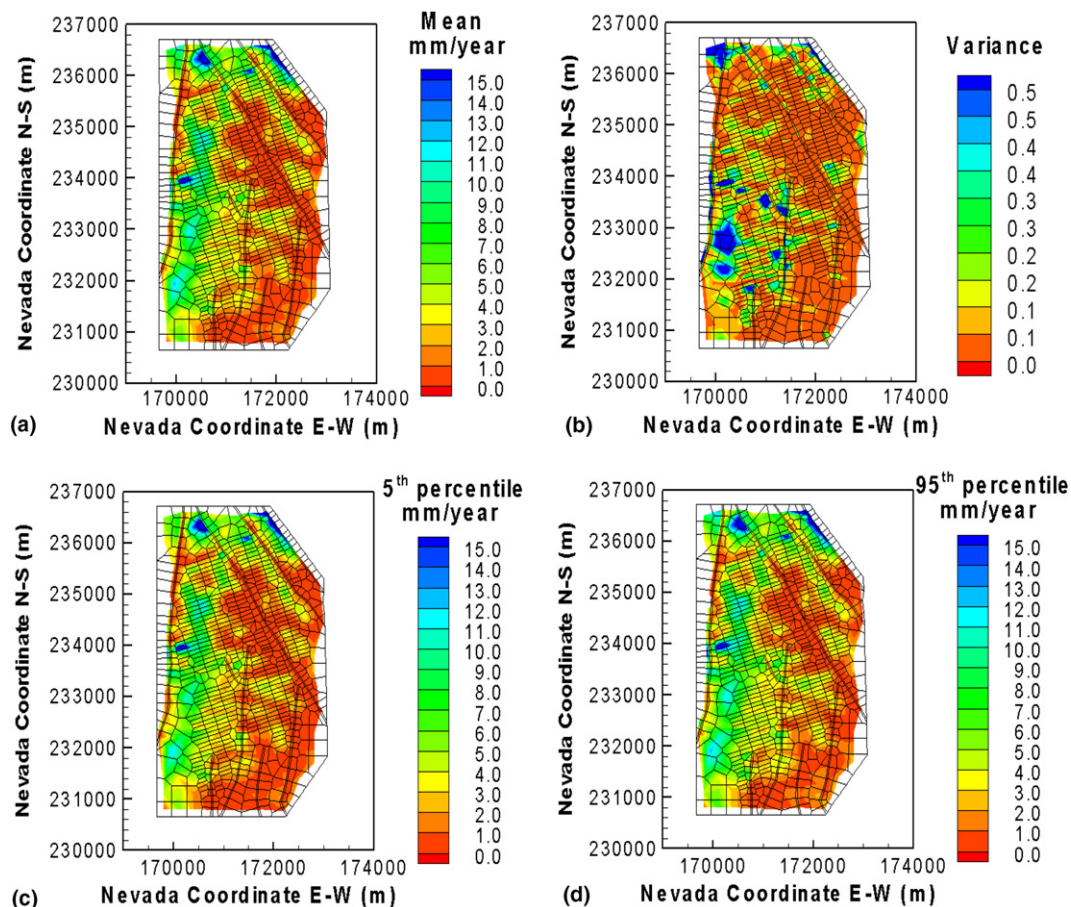

Fig. 8. (a) Mean, (b) variance, (c) 5th percentile, and (d) 95th percentile of simulated percolation fluxes at the repository horizon.
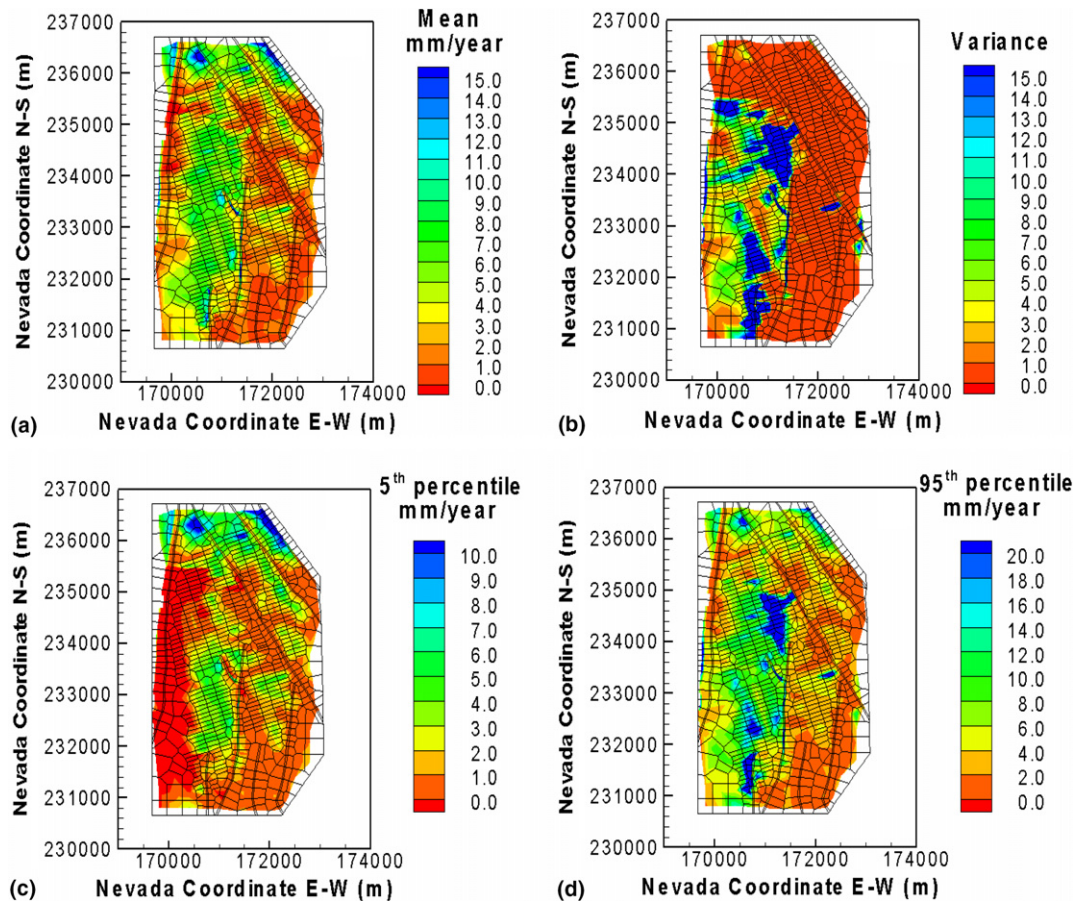
Fig. 9. (a) Mean, (b) variance, (c) 5th percentile, and (d) 95th percentile of simulated percolation fluxes at the water table.

tile in the simulated percolation flux at the repository horizon. Fig. 9 does the same at the water table. The mean percolation flux at the repository horizon (Fig. 8a) is similar to the surface infiltration (Fig. 2), indicating a small lateral movement of infiltrated water during the process of water traveling from the surface to the repository level. However, a comparison of Figs. 9a and 2 shows that the high-infiltration zone (denoted by dark "green" areas) moves eastward, indicating a significant lateral movement of infiltrated water.

Variance in percolation flux at the proposed repository horizon (Fig. 8b) is small. The largest variance occurs in the high-infiltration zone and at its eastern edge where the eastward movement occurs. Consistent with the small variance, the difference between the 5th and 95th percentiles (Fig. 8c and d) of the percolation flux is small, suggesting small predictive uncertainty in percolation flux caused by uncertainty in permeability. However, as shown in Fig. 9b, predictive uncertainty in percolation flux at the water table is large. The largest uncertainty also occurs in the high-infiltration zone and at its edge. The 5th and 95th percentiles (Fig. 9c and d) of percolation flux at the water table differ significantly, and this difference explains the variance distribution in Fig. 9b. For example, the two zones of large variance in Fig. 9b are attributed to the

two zones (marked in blue) of large percolation flux appearing at the middle and bottom of the simulation domain in the 95th-percentile map but not the 5th-percentile map. Although the variance in percolation flux is significantly larger at the water table than at the repository horizon, Fig. 5b shows that uncertainty in permeability near the water table is not significantly larger than near the repository zone. The large variance of percolation flux at the water table may be attributed to the accumulation of predictive uncertainty from the domain surface to its bottom, since infiltration rate is given as a deterministic condition at the domain surface.

4.2. Uncertainty assessment of radionuclide transport

Radionuclide transport uncertainty is assessed with two tracers in the present study: conservative (nonadsorbing) tracer, ^{99}Tc, and reactive (adsorbing) tracer, ^{237}Np. The sorption coefficients associated with neptunium (^{237}Np) are generated in Section 3 for the three rock types including devitrified, vitric, and zeolitc tuffs based on the measurements given in [27]. The transient transport simulation is conducted for 1,000,000 years. Initially, a constant concentration source is released instantaneously from the fracture continuum gridblocks representing the repository (Fig. 1).

4.2.1. Assessment of travel-time uncertainty for conservative and reactive tracers

One of the important factors in assessing performance of the proposed high-level nuclear waste repository at Yucca Mountain is radionuclide travel times from the repository to the water table. Fig. 10a and b plots the fractional breakthrough curves of cumulative mass arriving at the water table for the conservative (^{99}Tc) and reactive (^{237}Np) tracers, respectively. The effect of sorption is apparent in that the conservative tracer (^{99}Tc) travels about two orders of magnitude faster than the reactive tracer (^{237}Np). For example, the mean travel times corresponding to 50% mass fraction breakthrough are 3500 and 100,000 years for ^{99}Tc and ^{237}Np, respectively. For both tracers, the mean and 50th-percentile simulated breakthrough curves are close to the deterministic curve, especially for the conservative tracer, which does not have the sorption coefficient.

The 5th- and 95th-percentiles (uncertainty bounds) breakthrough curves in Fig. 10 show that the travel time of the reactive tracer (^{237}Np) is more uncertain than the travel time of the conservative tracer (^{99}Tc), owing to the uncertain sorption coefficient of ^{237}Np. For example,

Fig. 10a shows that at 1,000,000 years almost all ^{99}Tc flows out of the UZ into groundwater, while Fig. 10b shows that at 1,000,000 years 78% and 94% of the total mass of ^{237}Np flows into groundwater at the 5th- and 95th-percentile levels, respectively. Table 5 lists the travel times of 10%, 25%, 50%, 75%, and 90% for mass fraction breakthrough obtained from the mean, 5th-, and 95th-percentile breakthrough curves. The ranges of travel time between the 5th and 95th percentiles are significantly larger for the reactive tracer than for the conservative tracer. For example, it takes the reactive tracer 2.0×10^4 years (95th percentile) to 2.75×10^5 years (5th percentile) to flow 50% of the mass into the groundwater, whereas it only takes the conservative tracer 8.22×10^2 years (95th percentile) to 7.17×10^3 years (5th percentile). This indicates that the travel time prediction is more uncertain for the reactive tracer than for the conservative tracer. Fig. 10a shows that for the conservative tracer the range in uncertainty bounds first increases and then decreases with time. Whereas, Fig. 10b shows that for the reactive tracer the travel time uncertainty is of the same magnitude during the entire simulation period of 1,000,000 years. This also is due to the effect of the random sorption coefficient, which retards the travel of the reactive tracer and renders the corresponding travel time prediction more uncertain. This information can be used directly for risk analysis and monitoring network design. For example, monitoring radionuclide transport needs to last longer for the reactive tracer than for the conservative tracer.

4.2.2. Assessment of uncertainty of spatial distribution of radionuclide plumes

In addition to breakthrough curves, normalized cumulative mass arrival at the water table is calculated to eval-
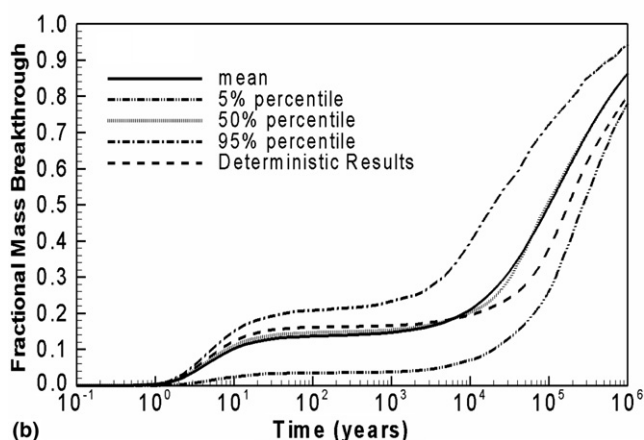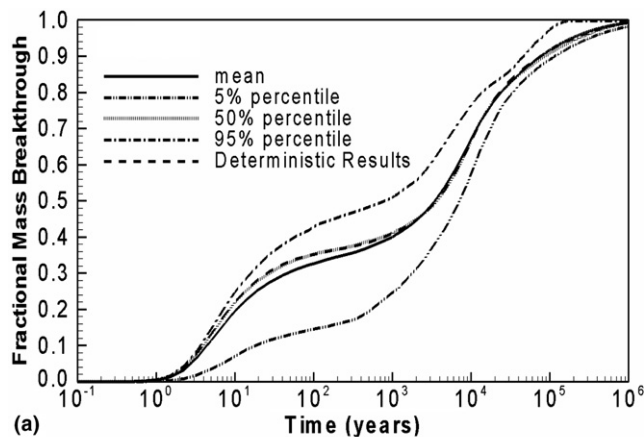

Fig. 10. Simulated breakthrough curves of cumulative mass arriving at the water table for (a) the conservative tracer (^{99}Tc) and (b) the reactive tracer (^{237}Np).

Table 5
Comparison of mean, 5th, and 95th percentiles of simulated travel time of the conservative (^{99}Tc) and reactive (^{237}Np) tracers arriving at water table at 10%, 25%, 50%, 75% and 90% mass fraction breakthrough (1.87E+1 reads as 1.87×10^1)

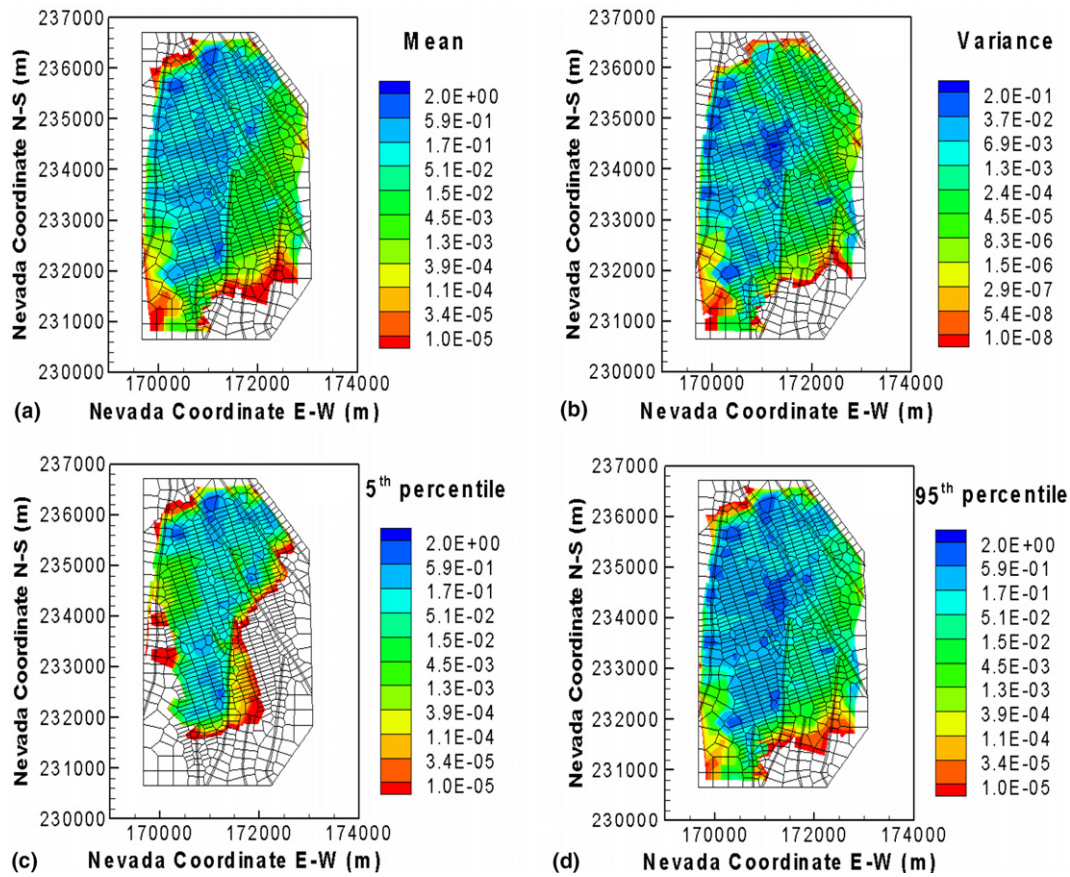| Breakthrough curves	Mass fraction (%)	Travel time (years)	
		Conservative tracer (^{99}Tc)	Reactive tracer (^{237}Np)
5th percentile	10	1.87E+1	1.99E+4
	25	1.08E+3	9.40E+4
	50	7.17E+3	2.75E+5
	75	2.32E+4	8.38E+5
	90	1.17E+5	>1.00E+6
Mean	10	4.47	9.70
	25	1.90E+1	1.72E+4
	50	3.50E+3	1.02E+5
	75	1.62E+4	4.26E+5
	90	7.71E+4	>1.00E+6
95th percentile	10	3.86	5.34
	25	1.03E+1	1.98E+3
	50	8.22E+2	2.00E+4
	75	9.00E+3	1.29E+5
	90	4.70E+4	5.80E+5

Fig. 11. (a) Mean, (b) variance, (c) 5th percentile, and (d) 95th percentile of normalized cumulative mass arrival contours of the reactive tracer (^{237}Np) at the water table after 1,000,000 years.

uate the spatial distribution of the tracers, which can help estimate the potential locations of high-radionuclide concentration. The cumulative mass arrival is the cumulative mass arriving at each cell of the water table over time, normalized by the total mass of the released radionuclide from the repository [35]. Fig. 11 plots (a) mean, (b) variance, (c) 5th percentile, and (d) 95th percentile of the normalized cumulative mass arrival contours of the reactive tracer (^{237}Np) at 1,000,000 years. The high-concentration zone (denoted in blue) in the mean mass arrival map (Fig. 11a) is beneath the footprint of the repository horizon marked by dots in Fig. 1. Spreading of the plume results from molecular diffusion (mechanical dispersion is inactivated in the numerical model) and lateral flow in the model domain. Comparing the variance map of mass arrival (Fig. 11b) with the map of percolation flux (Fig. 9b) shows that the two maps have a similar pattern and the high-variance zones in the two figures are at the same locations, indicating that variance in radionuclide transport is partly determined by variance in the flow. In addition, comparing the 5th and 95th percentiles of cumulative mass arrival (Fig. 11c and d) with the 5th and 95th percentiles of percolation flux at the water table (Fig. 9c and d) shows that high-mass arrival zones correspond to the high-flux zones. This further suggests the correlation

between uncertainties in radionuclide transport and percolation flux, implying that reducing percolation flux uncertainty leads to reduction in radionuclide transport uncertainty.

Fig. 12a–d plots the variance in cumulative mass arrival for the conservative (^{99}Tc) and reactive (^{237}Np) tracers at 1000 and 1,000,000 years. As "snapshots" of the two tracers at the two times, the four figures contain information on radionuclide transport uncertainty that cannot be seen from the breakthrough curves in Fig. 10. At 1000 years, the overall variance in mass arrival for the conservative tracer (Fig. 12a) is larger than that for the reactive tracer (Fig. 12c) and covers a larger area of breakthrough (almost the entire area directly below the repository footprint), since the conservative tracer moves faster. For the two tracers, the variance in the northern part of the water table is larger than in the southern part, suggesting that fast-flow paths may exist in the northern part. At 1,000,000 years, the variance maps of mass arrival for the two tracers are almost identical, because about 90–100% of both tracers has arrived at the water table at this time. Overall, the spatial distribution of radionuclide variance spreads larger with time, but the magnitude of variance decreases since the tracers flow out of the UZ with time.
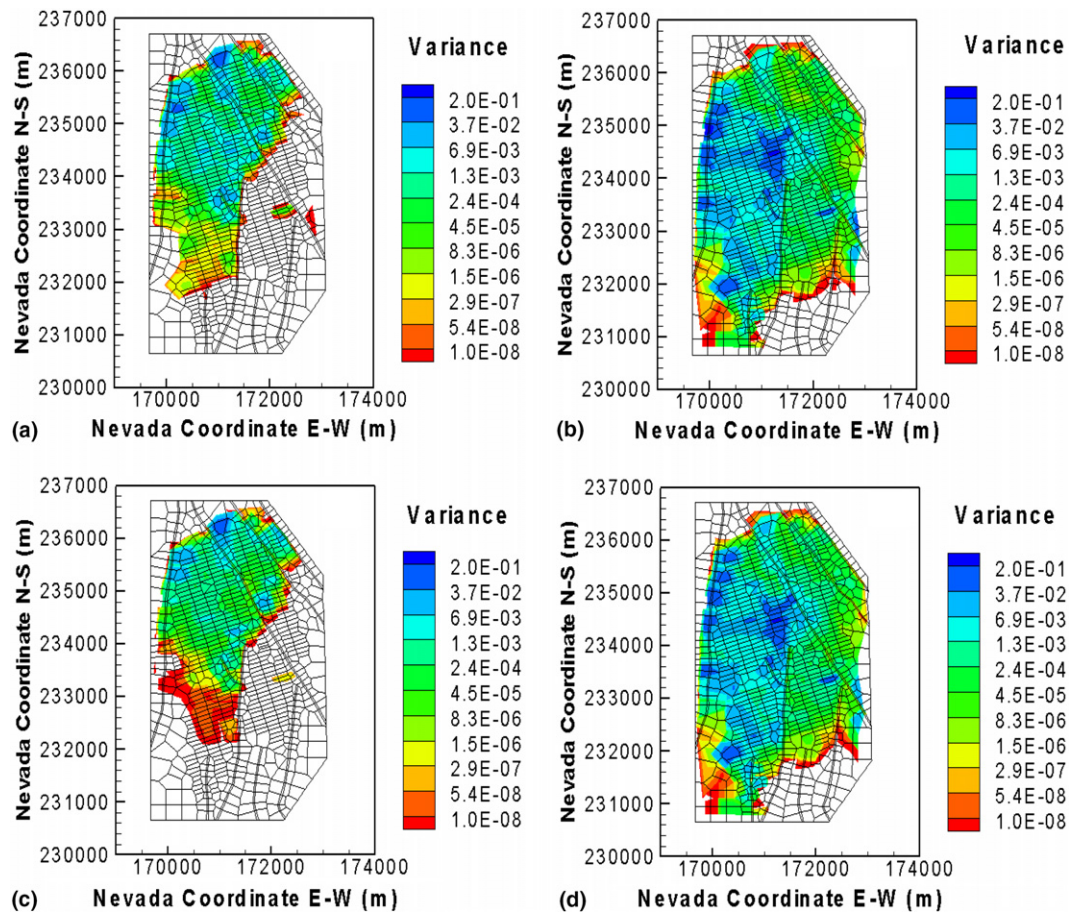
Fig. 12. Variance of normalized cumulative mass arrival of (a) ^{99}Tc at 1000 years, (b) ^{99}Tc at 1,000,000 years, (c) ^{237}Np at 1000 years, (d) ^{237}Np at 1,000,000 years at the water table.

5. Conclusions

This study presents our effort to assess uncertainty for unsaturated flow and radionuclide transport at the Yucca Mountain UZ. Matrix permeability, porosity, and sorption coefficient are treated as random variables, and their distributions are identified based on site measurements and model calibration results. Seven transformations (including three transformations from the Johnson system and four classical re-expressions) are applied to the measurements, and the Lilliefors test is used to select the best transformation at a certain significance level. The mean permeability is further adjusted based on model calibration results for better model predictions. Distributions of matrix porosity and sorption coefficients are determined solely from site measurements. The statistical correlation (measured by the Spearman rank correlation coefficient) between the matrix permeability and porosity is incorporated in the random field generation. Random fields generated using the Latin Hypercube Sampling (LHS) method agree well with the measurements, and 200 realizations are sufficient to yield representative distribution functions for the three random parameters.

A 3-D mountain-scale UZ flow and transport model is employed to conduct 200 Monte Carlo simulations using the numerical codes EOS9 and T2R3D of the TOUGH2 family. Mean, variance, and 5th-, 50th-, and 95th-percentile quantities of interest are evaluated. The mean and 50th percentile serve as the mean predictions, while their associated predictive uncertainty is measured by variance and the 5th and 95th percentiles (also known as uncertainty bounds). The mean predictions of matrix liquid saturation and water potential are in reasonable agreement with corresponding measurements, and the uncertainty bounds include a large portion of the measurements, suggesting that data variability can be partially explained by parametric uncertainty. Whereas mean percolation flux at the repository horizon is similar to surface infiltration (a slight eastward lateral movement is observed), mean percolation flux at the water table is significantly different, with significant eastward movement observed in the high-infiltration zone. While the largest uncertainties occur at the eastern edges of the high-percolation flux at both the water table and repository horizon, the uncertainty of percolation flux predictions is significantly larger at the water table. This suggests that site characterization at locations between the repository horizon and the water table will reduce uncertainty in the percolation flux prediction.

Radionuclide transport simulations are conducted for the conservative (nonadsorbing) tracer, ^{99}Tc, and the reac-

tive (adsorbing) tracer, [237]Np. In comparison with the conservative tracer, the arrival time of the reactive tracer from the repository horizon to the water table is delayed by chemical sorption. Because of the random sorption coefficient for the reactive tracer, travel-time uncertainty in the reactive tracer is significantly larger than travel-time uncertainty for the conservative tracer. Examining the snapshots of variance maps for radionuclide concentration at 1000 and 1,000,000 years shows that the spatial distribution of radionuclide variance spreads larger with time, but the magnitude of the variance decreases since tracers flow continuously out of the UZ. The present study also shows that uncertainty in radionuclide transport is related closely to uncertainty in percolation flux, suggesting that reducing the former entails reduction in the latter.

Acknowledgements

References

[1] Ahlers CF, Bandurraga TM, Bodvarsson GS, Chen G, Finsterle S, Wu YS. Summary of model calibration and sensitivity studies using the LBNL/USGS three-dimensional unsaturated zone site-scale model. Yucca Mountain site characterization project report, Milestone 3GLM107M, Lawrence Berkeley National Laboratory, Berkeley, CA, 1995.

[2] Ahlers CF, Finsterle S, Bodvarsson GS. Characterization and prediction of subsurface pneumatic response at Yucca Mountain, Nevada. J Contam Hydrol 1999;38(1–3):47–68.

[3] Bardurraga TM, Bardvarsson GS. Calibrating hydrogeologic properties for the 3-D site-scale unsaturated zone model at Yucca Mountain, Nevada. J Contam Hydrol 1999;38(1–3):5–46.

[4] Bowen WM, Bennett CA. Statistical methods for nuclear material management. Report NUREG/CR-4604, Battelle Pacific Northwest laboratory, Richland, WA, 1988.

[5] Carsel RF, Parrish RS. Developing joint probability distributions of soil water retention characteristics. Water Resour Res 1988;24(5):755–69.

[6] Dagan G. Flow and transport in porous formations. Berlin: Springer-Verlag; 1989.

[7] Flint LE. Characterization of hydrogeologic units using matrix properties, Yucca Mountain, Nevada. US Geol Surv Water-Resour Invest Report, 97-4243, 1998.

[8] Flint LE. Physical and hydraulic properties of volcanic rocks from Yucca Mountain, Nevada. Water Resour Res 2003;39(5):1–13.

[9] Gelhar LW. Stochastic subsurface hydrology. Englewood Cliffs: Prentice-Hall; 1989.

[10] Helton JC, Davis FJ. Latin Hypercube Sampling and the propagation of uncertainty in analyses of complex systems. Reliab Eng Syst Safety 2003;81:23–69.

[11] Hu BX, Wu J, Shirley C, Zhang D. A numerical method of moments for reactive solute transport in physically and chemically nonstationary formations: linear equilibrium sorption with random Kd. Stoch

Environ Res Risk Assess 2004;20:46–63. doi:10.1007/s00589-003-0253-5.

[12] Illman WA, Hughson DL. Stochastic simulations of steady state unsaturated flow in a three-layer, heterogeneous, dual continuum model of fractured rock. J Hydrol 2005;307:17–37.

[13] Iman RL, Conover WJ. A distribution-free approach to inducing rank correlation among input variables. Commu Statist Simul Comput 1982;11(3):311–34.

[14] Iuzzolino H. Users Manual (Rev 00) for LHS, Version 2.51. Civilian Radioactive Waste Managemenet System Management and Operating Contractor, MOL.20040210.0391, Albuquerque, New Mexico, 2003.

[15] Johnson NL, Kotz S. Distributions in statistics: continuous univariate distributions, vol. 1. Boston: Houghton Miffin Company; 1970.

[16] Liu HH, Ahlers CF, Mukhpadhayay S, Wu YS. Calibrated properties model. Report MDL-NBS-HS-000003 REV 01, Lawrence Berkeley National Laboratory, Berkeley, CA and CRWMS M&O, Las Vegas, Nevada, 2003.

[17] Liu HH, Zhu M, Persoff P, Gilkcrson K, Wu YS, Wang JSY. Analysis of Hydrologic Properties Data. Report MDL-NBS-HS-000014 REV00, Lawrence Berkeley National Laboratory, Berkeley, CA and CRWMS M&O, Las Vegas, Nevada, 2003.

[18] Mallants D, Jacques D, Vanclooster M, Diels J, Feyen J. A stochastic approach to simulate water flow in a macroporous soil. Geoderma 1996;10:299–324.

[19] Mckay MD, Beckman RJ, Conover WJ. A comparison of three methods for selecting values of input variables in the analysis of output from a computer code. Technometrics 1979;21(2):239–45.

[20] Meyer PD, Rockhold, ML, Gee GW. Uncertainty analysis of infiltration and subsurface flow and transport for SDMP sites. NUREG/CR-6565, PNNL-11705, US Nuclear Regulatory Commission, Office of Nuclear Regulatory Research, Washington, DC, 1997.

[21] Neuman SP. Maximum likelihood Bayesian averaging of alternative conceptual-mathematical models. Stoch Environ Res Risk Assess 2003;17(5):291–305. doi:10.1007/s00477-003-0151-7.

[22] Nichols WE, Freshley MD. Uncertainty analyses of unsaturated zone travel time at Yucca Mountain. Groundwater 1993;31(2):293–301.

[23] Pan F. Uncertainty analysis of radionuclide transport in the unsaturated zone at Yucca Mountain. Master Thesis, University of Nevada, Las Vegas, 2005. p. 128.

[24] Pruess K. TOUGH2—a general-purpose numerical simulator for multiphase fluid and heat flow. Report LBL-29400, Lawrence Berkeley National Laboratory, Berkeley, CA, 1991.

[25] Robinson BA, Li C, Ho CK. Performance assessment model development and analysis of radionuclide transport in the unsaturated zone, Yucca Mountain, Nevada, 2003.

[26] Swiler LP, Wyss GD. A user's guide to Sandia's Latin Hypercube Sampling software: LHS UNIX library/standalone version. Technical Report SAND2004-2439, Sandia National Laboratories, Albuquerque, NM, 2004.

[27] Triay IR, Meijer A, Conca JL, Kung KS, Rundberg RS, Strietelmeier BA, et al. Summary and synthesis report on radionuclide retardation for the Yucca Mountain site characterization project. Report LA-13262-MS, Los Alamos National Laboratory, ACC: MOL.19971210.0177, Los Alamos, New Mexico, 1997.

[28] Viswanathan HS, Robinson BA, Valocchi AJ, Triay IR. A reactive transport model of neptunium migration from the potential repository at Yucca Mountain. J Hydrol (Amsterdam) 1998;209:251–80.

[29] Wu J, Hu BX. Three-dimensional method of moments for linear equilibrium-adsorbing solute transport in physically and chemically nonstationary formations. Math Geol 2004;36(2):261–87.

[30] Wu YS, Haukwa C, Bodvarsson GS. A modeling study of perched water phenomena in the unsaturated zone of Yucca Mountain, Nevada. J Contam Hydrol 1999;38(1–3):157–84.

[31] Wu YS, Haukwa C, Bodvarsson GS. A site-scale model for fluid and heat flow in the unsaturated zone of Yucca Mountain, Nevada. J Contam Hydrol 1999;38(1–3):185–217.

[32] Wu YS, Pruess K. Numerical simulation of non-isothermal multi-phase tracer transport in heterogeneous fractured porous media. Adv Water Resour 2000;23:699–723.

[33] Wu YS, Pan L, Zhang W, Bodvarsson GS. Characterization of flow and transport processes within the unsaturated zone of Yucca Mountain, Nevada, under current and future climates. J Contam Hydrol 2002;54:215–47.

[34] Wu YS, Zhang W, Pan L, Hinds J, Bardvarsson GS. Modeling capillary barriers in unsaturated fractured rock. Water Resour Res 2002;38(11):1253. doi:10.1029/2001WR00852.

[35] Wu YS, Lu G, Zhang K, Zhang G, Liu HH, Xu T, et al. UZ Flow Models and Submodels, Report MDL-NBS-HS-000006 REV02, Lawrence Berkeley National Laboratory, Berkeley, CA and CRWMS M&O, Las Vegas, Nevada, 2004.

[36] Wu YS, Lu G, Zhang K, Bodvarsson GS. A mountain-scale model for characterizing unsaturated flow and transport in fractured tuffs of Yucca Mountain. Vadose Zone J 2004;3:796–805.

[37] Xu J, Hu BX. A numerical Eulerian method of moment for solute transport in a nonstationary dual-porosity medium. Adv Water Resour 2004;27(3):207–22.

[38] Ye M, Neuman SP, Meyer PD. Maximum likelihood Bayesian averaging of spatial variability models in unsaturated fractured tuff. Water Resour Res 2004;40:W05113. doi:10.1029/2003WR002557.

[39] Ye M, Neuman SP, Guadagnini A, Tartakovsky DM. Nonlocal and localized analyses of conditional mean transient flow in bounded, randomly heterogeneous porous media. Water Resour Res 2004;40:W05104. doi:10.1029/2003WR002099.

[40] Zhang D, Winter CL. Nonstationary stochastic analysis of steady state flow through variably saturated, heterogeneous media. Water Resour Res 1998;34(5):1091–100.

[41] Zhang D. Nonstationary stochastic analysis of transient unsaturated flow in randomly heterogeneous media. Water Resour Res 1999;35(4):1127–41.

[42] Zhang D. Stochastic methods for flow in porous media: coping with uncertainties. San Diegeo: Academic Press; 2002.

[43] Zhang K, Wu YS, Houseworth JE. Sensitivity analysis of hydrological parameters in modeling flow and transport in the unsaturated zone of Yucca Mountain. Hydrogeol J, in press.

[44] Zhang Y, Pinder GF, Herrera GS. Least cost design of groundwater quality monitoring networks. Water Resour Res 2005;41:W08412. doi:10.1029/2005WR003936.

[45] Zhou Q, Liu HH, Bodvarsson GS, Oldenburg CM. Flow and transport in unsaturated fractured rock: effects of multiscale heterogeneity of hydrogeologic properties. J Contam Hydrol 2003;60:1–30.